Magnetic properties of fcc and σ phases in equiatomic and off-equiatomic high-entropy Cantor alloys

Özge Özgün,[1] David Koch,[2] Aslı Çakır,[3] Tolga Tavşanoğlu,[3] Wolfgang Donner,[2] Michael Farle,[4] and Mehmet Acet[4]

[1]*Max-Planck-Institut für Eisenforschung GmbH, 40237 Düsseldorf, Germany*
[2]*Fachbereich Material- und Geowissenschaften, TU-Darmstadt, 64287 Darmstadt, Germany*
[3]*Department of Metallurgical and Materials Engineering, Muğla Sıtkı Koçman University, 48000 Muğla, Turkey*
[4]*Faculty of Physics and Center for Nanointegration (CENIDE), Universität Duisburg-Essen, 47048 Duisburg, Germany*

(Received 20 June 2022; revised 18 October 2022; accepted 12 December 2022; published 19 December 2022)

The equiatomic face-centered-cubic (fcc) high-entropy alloy CrMnFeCoNi has a valence electron concentration of 8 electrons per atom, equivalent to that of Fe. Its ground-state properties are similar to that of fcc-Fe and exhibits the anti-Invar effect at finite temperatures. It additionally exhibits various magnetic interactions at low temperatures which are not fully understood. To resolve this, we prepare and investigate the magnetic and structural properties of off-equiatomic $Cr_{20+x}Mn_{20}Fe_{20}Co_{20}Ni_{20-x}$ high-entropy alloys with $0 \leqslant x \leqslant 20$ at.% by making use of the composition-dependent transformation from the fcc to the σ phase with increasing x. We employ x-ray diffraction, scanning electron microscopy, magnetization, and microhardness studies. The results suggest that these alloys order antiferromagnetically around 75–90 K before entering into a spin-frozen state below 40 K.

DOI: 10.1103/PhysRevB.106.214422

I. INTRODUCTION

High-entropy alloys (HEAs) generally consist of five or more elements in near-equiatomic compositions [1,2] and are of particular interest because of their exceptional mechanical properties such as high ductility and high strength—both at high and low temperatures—and corrosion resistance [3–6]. Although having a high configurational entropy, HEAs stabilize in simple structures such as face-centered cubic (fcc) and body-centered cubic (bcc), and can be prepared in many combinations of transition-metal elements [7] as well as in transition-metal/main-group-element combinations. They can also stabilize in the more complex tetragonal σ phase having 30 atoms per unit cell. The σ phase occurs particularly when elements of the early transition metals such as Mo, Nb, and Ti are introduced into the alloy. This increases the hardness as well as the brittleness [8]. The vast number of studies dealing with the mechanical properties of HEAs having the cubic phases have been collected in a number of review articles introducing discussions on the relationship between mechanical and electronic properties as well as providing a historical background and possible routes for tailoring their properties [9–11].

In addition to the structural and favorable mechanical properties, HEAs also exhibit interesting magnetic properties which have been less dealt with. These would go hand-in-hand with the structural and mechanical properties through the electronic structure. Although there have been a number of theoretical and experimental studies on the magnetic properties even on the archetype HEA, namely the equiatomic Cantor alloy CrMnFeCoNi, there are still remaining issues concerning the ground-state properties of this material in the fcc and σ phase that are yet to be resolved. The magnetic properties of the σ phase of these alloys are little known.

The fcc-Cantor alloy has the same valence-electron concentration (e/a: electrons per atom) as fcc-Fe with $(e/a) = 8$ and exhibits temperature-dependent properties that are actually predicted for fcc-Fe [12]. Looking closer at the temperature-dependent magnetic properties of the Cantor alloy, one should be able to extract information on its magnetic properties by comparing the measured features to those predicted for fcc-Fe. In particular, there are two features in the temperature dependence of the magnetization at low temperatures [13]. One is related to magnetic frustration around 10 K and the other occurs around 80 K. The reason for the latter is not as well pinpointed. We argue that this feature is related to AF ordering which is similar to the expected AF ordering in fcc-Fe had it been stable [14]. Investigating the magnetic properties of off-equiatomic Cantor alloys as a function of composition can provide information on this magnetic property while the structure progresses from the pure fcc to the pure σ phase. This can give a better explanation for the feature around 80 K as well as information on the magnetic properties of the σ phase. For this we have prepared and investigated the (e/a) dependence of the structural and magnetic properties of the alloy-series $Cr_{20+x}Mn_{20}Fe_{20}Co_{20}Ni_{20-x}$ in the nominal concentration range $0 \leqslant x \leqslant 20$, $x = 0$ being the Cantor alloy.

Before presenting and discussing the data, we give here a brief background and a review on the current state of knowledge on the structural and magnetic properties of 3*d* HEAs and in particular that of the electronically fcc-Fe-equivalent Cantor alloy to provide more detail for the aim of the present work.

II. BACKGROUND

A. Cubic and hexagonal HEAs

Regarding ground-state properties of equiatomic HEAs, Ma *et al.* have taken into hand the study of structural and magnetic properties and compared the total energies and the magnetic coupling in the hexagonal close packed (hcp), fcc, and bcc states [15]. They find that the a nonmagnetic hcp state is most stable and argue that this phase is not observed in experiment because of kinetic limitations of a phase transformation from fcc to hcp under experimental conditions. Dong *et al.* take into account longitudinal spin fluctuations in comparing the relative stability of the fcc and hcp phases and also report that the hcp phase is favored in the ground state [16]. However, from the experimental side it is found that only under high pressures (14 GPa) does the Cantor alloy indeed undergo a phase transformation to the hcp phase [17]. Experiments at ambient pressure indicate that the low-temperature structure of the Cantor alloy is fcc [13,18].

Schneeweiss *et al.* [13] report that determining the magnetic ordering of the individual elements is computationally demanding, but they were able to conclude from the results of calculations and Mössbauer experiments that the Cr magnetic moments align antiferromagnetically with respect to the Fe and Co atoms. This result along with the prediction that the Mn moments also align antiferromagnetically to Fe and Co display the complexity of the magnetic ordering taken up in HEAs [15]. These were verified by x-ray magnetic circular dichroism experiments, where it was shown that the direction of the magnetic moments on Cr in the Cantor alloy oppose the direction of the bulk total moment, whereas the total Mn moment is zero due to the equal amount of parallel and opposite alignment of the moments to the applied magnetic field [19].

Further experimental work was carried out by Koželj *et al.* who studied the low-temperature properties of an off-stoichiometric single-crystal Cantor alloy with high Mn deficiency (Mn 7.2 at. %) and found a magnetically frustrated state at low temperatures [20]. Their results on AC susceptibility measurements show a frequency dependence below the freezing temperature T_f around 20 K, but no frequency dependence at temperatures above 25 K that would be indicative of the presence of magnetic frustration effects. The results are somewhat different than those of Schneeweiss *et al.* perhaps due to the off-stoichiometry [13].

As to magnetic interactions, Šebesta *et al.* predict a disordered local moment state for the Cantor alloy with no long-range magnetic ordering [21]. Huang *et al.* investigated magnetic ordering in equiatomic medium- and high-entropy alloys and estimated their Curie temperatures T_C [22]. For the Cantor alloy, they report $T_C = 20$ K. This low value can be considered to be in agreement with experiment and the results of other theoretical works mentioned above. This has also been corroborated by Chaudhary *et al.* who have employed a combinatorial approach and investigated the magnetic properties of a broad spectrum of medium- and high-entropy alloys including alloys incorporating main group elements [23]. Combinatorial approaches have also been undertaken for studying the magnetic properties of Cu-incorporating HEAs, some which can acquire FM ordering [24].

Further theoretical studies on the magnetic properties of other HEAs beyond the Cantor alloy or compositionally modified Cantor alloys were also carried out [25,26]. These include replacing or substituting one of the elements in the Cantor alloy with another transition metal or a main group element with the objective of investigating temperature-dependent magnetic properties as well as ground-state properties.

The results of the experimental and theoretical works mentioned above show that the magnetic properties in the magnetically frozen state of the Cantor alloy are well understood to arise from magnetic frustration effects caused by the antiparallel coupling of the Cr moment to ferromagnetically coupled Fe, Co, and Ni, and the equal amount of parallel and antiparallel coupling of the Mn moment to the moments on these elements. A remaining issue related to magnetism of the fcc Cantor alloy is the feature observed in the temperature dependence of the magnetization at around 80–90 K, of which the origin is not clear. One of the aims of this work is to deal with this problem.

B. The σ phase

The unit cell of the tetragonal intermetallic σ phase contains 30 atoms per unit cell. In stainless steel this phase occurs as precipitates located at grain boundaries or within grains, and their varieties have been accordingly classified [27]. It leads to material hardening, which could be favorable under certain circumstances [28] and the compositional range of its stability is in general governed by e/a [29,30]. For the case of 3d HEAs, Laplanche *et al.* have studied the kinetics of σ-phase precipitation in a Cr-rich off-stoichiometric Cantor alloy [31]. The Cantor alloy itself is found to be highly stable in the fcc structure [32] and would undergo a transition to the σ phase when annealed around 700 °C for prolonged periods extending from months to years [33].

Much of the structural properties of the σ phase in HEAs have been thoroughly studied and it has been shown that its occurrence in transition metals can also be predicted [29]. As regard to the magnetic properties, some earlier magnetization and Mössbauer spectroscopy work on the σ-phase binaries Fe-V and Fe-Cr show that these order ferromagnetically below room temperature [34]. The magnetic properties of the σ phase in HEAs, on the other hand, has not been studied. This will be taken into hand in this work mainly by examining the gradual changes in the temperature and field dependencies of the magnetization $M(T)$ and $M(B)$, respectively, of $Cr_{20+x}Mn_{20}Fe_{20}Co_{20}Ni_{20-x}$.

C. Magnetoelastic properties and e/a: Similarities in the properties of the Cantor alloy and fcc-Fe

The principal elements used in HEAs are 3d metals, and these carry magnetic interactions so that if thoroughly understood, HEAs could open up new areas in the development of novel magnetic materials.

Much of the magnetic properties of HEAs can be accounted for by basic arguments based on the dependence of the magnetic moment and the magnetic transition temperature on e/a. In fact, most magnetic properties can be predicted on this basis allowing for the possibility of adjusting magnetic

and structural properties. A typical example of this is that the element Fe and the Cantor alloy $Cr_{20}Mn_{20}Fe_{20}Co_{20}Ni_{20}$ have the same (e/a) value of 8 so that the fcc-Cantor alloy should be electronically equivalent to fcc-Fe. On this basis, it can then be expected that fcc-Fe and the fcc-Cantor alloy exhibit similar measured features. Indeed, we had shown in a previous work that the Cantor alloy has ground-state properties that are similar to that of fcc-Fe [12]. This is seen particularly in the features of the temperature-dependent thermal expansion coefficient data, from which it can be understood that the Cantor alloy can carry similar anti-Invar properties as fcc-Fe and possesses moment-volume instabilities [35].

Based on these observations, we had extended our studies to design an alloy with an (e/a) value of about 8.7, at which Invar properties would be expected to stand out. To adjust this value we prepared a HEA with the stoichiometry $Mn_{12.1}Fe_{34.2}Co_{33.5}Ni_{12.3}Cu_{7.9}$. Its structural and magnetic properties showed indeed that the alloy carried Invar properties [36]. This provided further support that e/a governs the magnetoelastic properties of $3d$ alloys and compounds and also in multicomponent, compositionally complex HEAs. The (e/a) guide is mostly valid for $3d$ metals and its alloys but with some modifications it can also apply to interstitial $3d$ alloys and compounds, such as carbides and nitrides [37], as well as alloys and compounds including main group elements, such as Heusler alloys [38].

The Cantor alloy is an anti-Invar and mimics the properties of fcc-Fe, but unlike fcc-Fe it is stable throughout the solid-state temperature range. Therefore, understanding its low-temperature magnetic properties may bring about new information on the magnetic properties in the fcc state of $3d$ metals and alloys with e/a around 8. The presence of a moment-volume instability between a low-spin [LS or antiferromagnetic (AF)], low-volume state with nearly zero moment and a high-spin (HS), high-volume state with $\mu = 2.8\ \mu_B$ along with the stability of the fcc state up to high temperatures brings about the possibility to construct a magnetic material with a large magnetic moment paving way to synthesizing new functional magnetic materials.

III. EXPERIMENT

Polycrystalline ingots were prepared by arc melting under Ar atmosphere in a Cu crucible using 99.95% pure Cr, Mn, Fe, Co, and Ni. The nominal compositions are $Cr_{20+x}Mn_{20}Fe_{20}Co_{20}Ni_{20-x}$ ($x = 0$, 2, 5, 10, 15, 20). These are designated as S1, S2,..., S6. The melting process was repeated four times. A further homogenization was carried out at 900 °C for 14 days under Ar atmosphere in sealed quartz tubes. This annealing temperature is reported to be optimum for generating the σ phase. Afterwards, the alloys were quenched in water at room temperature. The chemical compositions and homogeneities of the samples were determined by energy dispersive x-ray analysis (EDX) using a scanning electron microscope (SEM).

X-ray diffraction (XRD) was carried out at room temperature (RT) and as a function of temperature. Cu $K\alpha$ radiation was used for the RT measurements. The results were refined using Le Bail refinement with Jana [39]. The measurements were carried out on bulk samples for S1–S5, since these samples are not suitable for obtaining powders, and on a powder sample for S6, for which powder is readily obtained.

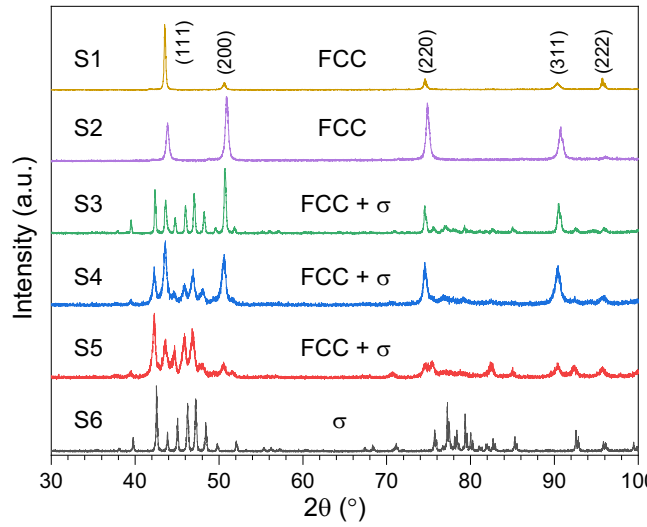

FIG. 1. XRD patterns of the investigated alloys homogenized at 900 °C for 14 days. Only fcc peaks are observed for S1 and S2. σ and fcc phases coexist in S3, S4, and S5. S6 with highest Cr content is single-phase σ. Miller indices are given for the fcc phase for S1.

Temperature-dependent XRD was performed using a custom-built diffractometer with a closed-cycle cold-finger He cryostat, employing Mo $K\alpha$ radiation and a Mythen 1 K R detector [40]. Measurements were run on a bulk and a powder sample. The bulk sample was fixed with thermally conductive adhesive on a sample support. NIST Si 640d was added onto the surface for correcting geometric errors. The sample was rotated by $\pm 7.5°$ during the measurements carried out in reflection. The powder sample was also mixed with NIST Si 640d and glued on a graphite foil and measured in transmission. The sample was rotated by $\pm 7.5°$ during the measurements. The data were evaluated using Le Bail refinement for the bulk sample and Rietveld refinement for the powder sample using FullProf software [41].

The Vicker hardnesses of alloys were measured using a Duroline-M microhardness tester under a test load of 3 N with 10 s dwell times. Magnetization measurements were carried out using a superconducting quantum interference device (SQUID) magnetometer in the temperature range $10 \leqslant T \leqslant 380$ K and in fields up to 5 T.

IV. RESULTS

We first show the results on the chemical and structural characterizations and subsequently the results on the magnetization and hardness measurements.

A. Chemical and structural characterization

The results of XRD studies seen in Fig. 1 show that the samples S1 and S2 close to the equiatomic composition are fcc with space group $Fm-3m$. The samples S1–S5 are bulk samples so that texturing is unavoidable. This leads to disproportionate peak intensities in XRD patterns as is the case particularly here for S2, where the (200) peak is more

TABLE I. Refined lattice parameters of fcc and σ phases.

Label	a_{fcc} (nm)	$(a, c)_\sigma$ (nm)	V_{at}^{fcc} (10^{-3} nm^3)	V_{at}^{σ} (10^{-3} nm^3)
S1	0.3601	–	11.67	–
S2	0.3597	–	11.63	–
S3	0.3599	$a = 0.8789, c = 0.4560$	11.65	11.74
S4	0.3603	$a = 0.8815, c = 0.4580$	11.69	11.85
S5	0.3600	$a = 0.8812, c = 0.4576$	11.66	11.84
S6	–	$a = 0.8808, c = 0.4559$	–	11.79

intense than the (111) peak. This, however, has little effect in determining the lattice parameters. As the Cr concentration increases at the expense of Ni, fcc and σ phases coexist as seen for samples S3, S4, and S5. A single σ phase is observed for S6. The σ phase is tetragonal with 30 atoms per unit cell with space group $P42/mnm$. The refined lattice parameters and the estimated atomic volume of the fcc and σ phases at room temperature are collected in Table I. For S6, $(e/a) = 7.1$, which is close to the value for $Fe_{50}Cr_{50}$.

The chemical compositions for the fcc and σ phases determined by EDX analysis, and the respective e/a values, are collected in Table II. The samples S1 and S2 with $(e/a) = 8$ and 7.9, respectively, are fcc with a nearly equiatomic composition. Whereas the chemical compositions of the σ phase in the dual-phase alloys S3, S4, and S5 are similar, the Cr and Ni compositions in the fcc phase vary.

The results of elemental mapping carried out for sample S3 is shown in Fig. 2. The lighter areas correspond to higher counts. The result shows that Mn, Fe, and Co are distributed more homogeneously than Cr and Ni. The intensity of Cr K_α radiation is high in regions where the Ni concentration is low. Thus, the Cr-rich regions are related to the σ phase, whereas the Ni-rich regions are fcc. This can also be seen from the chemical compositions of the two phases in Table II. Elemental mapping shows that all elements are evenly distributed in S6, therefore an image is not presented here.

B. The thermal expansions of the fcc and σ phases

The equiatomic Cantor alloy with $e/a = 8$ is known to exhibit the anti-Invar property as fcc-Fe [12]. This magnetoelastic property related to LS-HS thermal fluctuations appears as an enhancement in the thermal expansion and its temperature dependence and provides evidence for the presence of moment-volume instabilities in the ground state [16,35]. It has been shown that the temperature dependence of the thermal

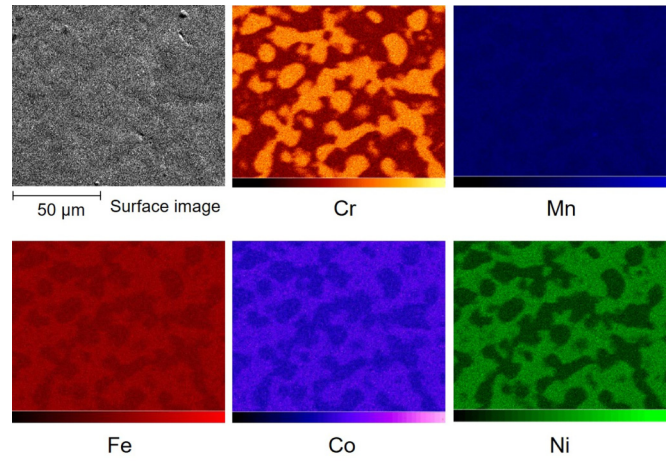

FIG. 2. Elemental mapping results for sample S3 taken from the area shown by the surface image. The lighter areas correspond to higher counts.

expansion coefficient $\alpha(T)$ of the Cantor alloy carries features similar to that of fcc-Fe. To show that this property is unique for the fcc-Cantor alloy among the alloz/series investigated, we compare its thermal expansion with that of the σ-phase alloy S6. For this we have obtained further XRD data as a function of temperature and estimated the temperature dependence of the lattice parameters of the fcc and σ phases in samples S2 and S6, respectively. Figure 3(a) shows the temperature dependence of the relative atomic-volume change referenced to 15 K $\Delta V/V_{15}$ for samples S2 (fcc) and S6 (σ), and Fig. 3(b) shows the temperature dependence of the c and a lattice parameters for sample S6. The error in determining $\Delta V/V_{15}$ is about the size of the data points, whereas an error bar is shown for S2, for which bulk polycrystalline samples were used. $\Delta V/V_{15}$ for S2 agree well with those in Ref. [13], and it is seen that the volume thermal expansion of S2 increases faster with increasing temperature than that of S6 as of about 150 K. The expansion being isotropic for S2, the linear thermal expansion can be expressed as $\Delta l/l_{15} = (1/3)\Delta V/V_{15}$, where l is the length. The coefficient of linear thermal expansion α around room temperature can be estimated to be about 17×10^{-6} K^{-1}, which is an enhanced α value with respect to a normal Grüneisen value of about 10×10^{-6} K^{-1} around room temperature and agrees with the values given in Refs. [12,42]. The σ phase is nonisotropic so that the a- and c-axis expansions are handled separately. We find $\alpha_a = \alpha_c \approx 11 \times 10^{-6}$ K^{-1} for the σ phase which are considerably less than that for sample S2. Therefore,

TABLE II. Chemical compositions and e/a values in fcc and σ phases in $Cr_{20+x}Mn_{20}Fe_{20}Co_{20}Ni_{20-x}$.

Label	Nominal x	fcc	$(e/a)_{fcc}$	σ phase	$(e/a)_\sigma$
S1	0	$Cr_{19.4}Mn_{21.3}Fe_{18.6}Co_{20.7}Ni_{20.0}$	8.0	–	–
S2	2	$Cr_{22.8}Mn_{19.6}Fe_{20.1}Co_{19.6}Ni_{17.9}$	7.9	–	–
S3	5	$Cr_{22.5}Mn_{20.9}Fe_{22.2}Co_{22.5}Ni_{11.9}$	7.8	$Cr_{41.5}Mn_{16.8}Fe_{18.9}Co_{17.9}Ni_{4.9}$	7.3
S4	10	$Cr_{28.0}Mn_{20.1}Fe_{19.7}Co_{22.0}Ni_{10.2}$	7.7	$Cr_{38.8}Mn_{18.5}Fe_{18.6}Co_{18.1}Ni_{6.0}$	7.3
S5	15	$Cr_{34.2}Mn_{19.7}Fe_{19.9}Co_{20.0}Ni_{6.2}$	7.4	$Cr_{39.9}Mn_{18.6}Fe_{18.7}Co_{18.7}Ni_{4.1}$	7.3
S6	20	–	–	$Cr_{44.6}Mn_{17.9}Fe_{18.7}Co_{18.8}$	7.1

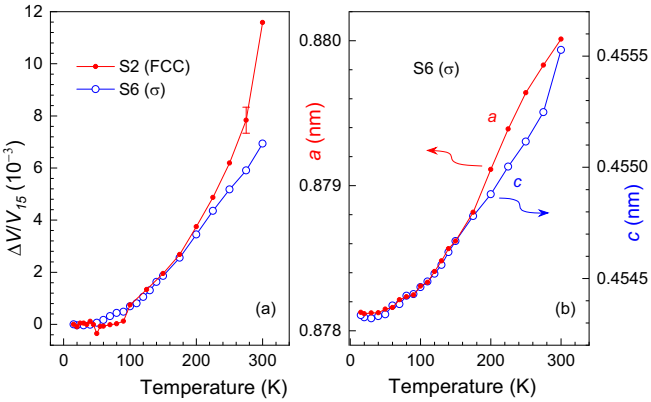

FIG. 3. Thermal expansion and temperature-dependent cell dimensions. (a) The temperature dependence of the relative change in the cell volume of samples S2 (fcc) and S6 (σ). (b) a and c lattice parameter of S6.

moment-volume instabilities are not expected to be present in the σ phase. This point is discussed in more detail in Sec. V.

C. Magnetization

Low-field (5 mT) temperature-dependent magnetization measurements $M(T)$ are carried out in the range $10 \leqslant T \leqslant 380$ K to reveal features related to the intrinsic magnetic interactions. The measurements were taken on warming from the zero-field-cooled (ZFC) state at 10 to 380 K and then, without removing the field, on field cooling (FC) from 380 to 10 K. The data are also taken under 100 mT, 1 T, 3 T, and 5 T with the same protocol to observe the changes in the features in $M(T)$ with changing measuring field. The results are presented in Figs. 4–9 along with the field dependence of the magnetization $M(B)$ at 10 K. $M(B)$ was obtained after cooling the sample in 5 T to 10 K to search for the presence of any shifted hysteresis loops that may be related to magnetic pinning effects. Common to $M(T)$ of all samples

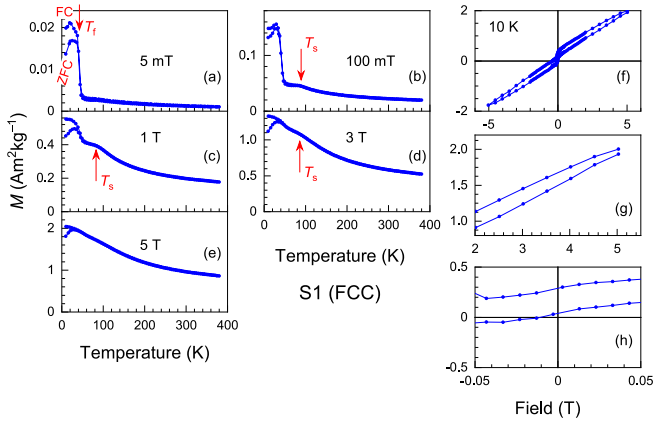

FIG. 4. $M(T)$ under 5 mT external field obtained under ZFC and FC conditions for S1. (a) 5 mT, (b) 100 mT, (c) 1 T, (d) 3 T, and (e) 5 T. The shoulder feature at T_s is marked by the arrows. The $M(B)$ loop in (f) does not retrace at high-field ends as detailed in (g) so that $M(B)$ is displaced around the origin (h). T_f denotes the freezing temperature

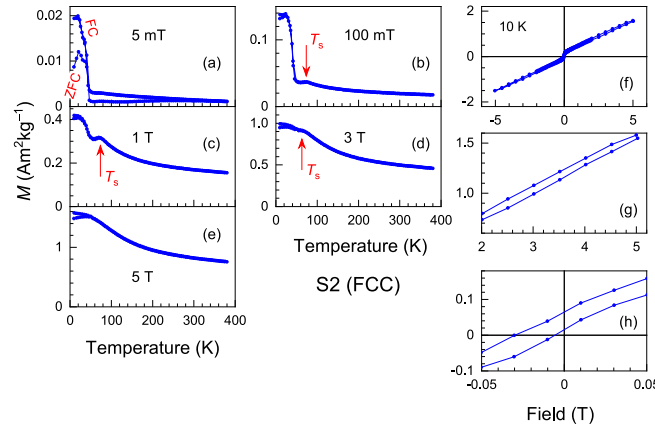

FIG. 5. $M(T)$ under 5 mT external field obtained under ZFC and FC conditions for S2. (a) 5 mT, (b) 100 mT, (c) 1 T, (d) 3 T, and (e) 5 T. The shoulder feature at T_s is marked by the arrows. The $M(B)$ loop in (f) does not retrace at high-field ends as detailed in (g) so that $M(B)$ is displaced around the origin (h).

is the enhanced paramagnetic response due to the anti-Invar effect observed in the high-temperature regime ($T > 200$ K) giving rise to a finite magnetization especially for the higher measurement fields. This response is expected to be related to the occurrence of thermally induced low-spin to high-spin fluctuations strengthening with increasing temperature [12].

Two features are observed at low temperatures in the $M(T)$ data of S1–S5. The first is the splitting in the FC and ZFC curves at the magnetic freezing temperature T_f of about 40 K followed by a rapid decrease in $M(T)$ with increasing temperature starting around 45–50 K depending on the composition. The branches are labeled as FC and ZFC in red in Figs. 4–8, and T_f is shown by an arrow representatively in Fig. 4(a). The splitting persists up to the highest measuring fields for S1 and S2, although somewhat weaker for S2. It disappears for $B \geqslant 100$ mT for samples S3–S5 and is absent in the pure σ-phase sample S6. The splitting is likely caused by magnetic

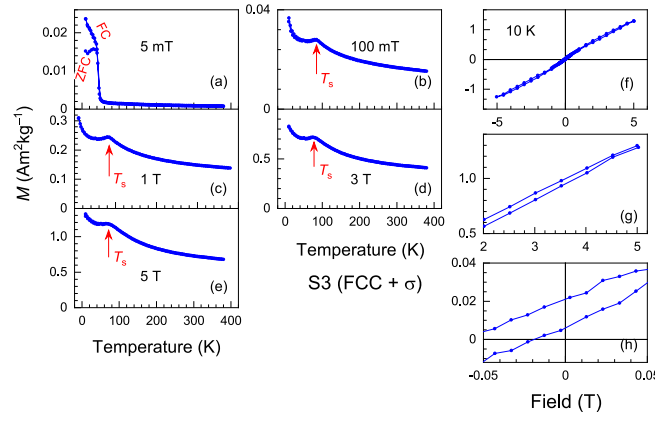

FIG. 6. $M(T)$ under 5 mT external field obtained under ZFC and FC conditions for S3. (a) 5 mT, (b) 100 mT, (c) 1 T, (d) 3 T, and (e) 5 T. The shoulder feature at T_s is marked by the arrows. The $M(B)$ loop in (f) does not retrace at high-field ends as detailed in (g) so that $M(B)$ is displaced around the origin (h).

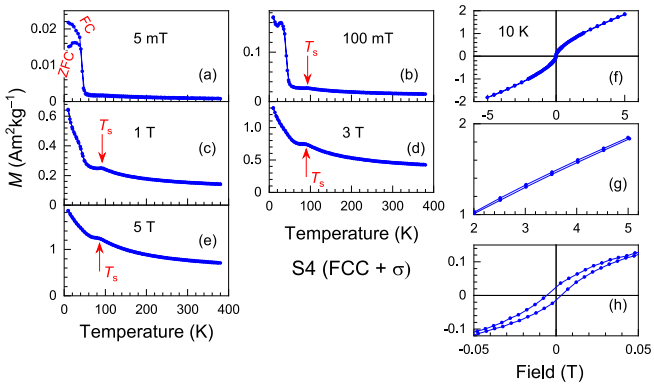

FIG. 7. $M(T)$ under 5 mT external field obtained under ZFC and FC conditions for S4. (a) 5 mT, (b) 100 mT, (c) 1 T, (d) 3 T, and (e) 5 T. The shoulder feature at T_s is marked by the arrows. The $M(B)$ loop in (f) does not retrace at high-field ends as detailed in (g) so that $M(B)$ is displaced around the origin (h).

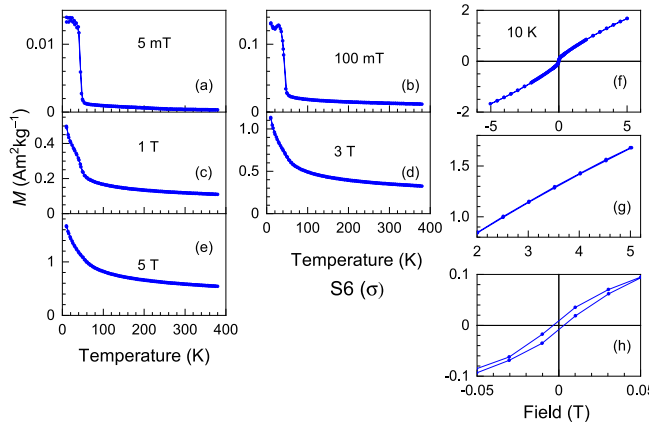

FIG. 9. $M(T)$ under 5 mT external field obtained under ZFC and FC conditions for S5. (a) 5 mT, (b) 100 mT, (c) 1 T, (d) 3 T, and (e) 5 T. No splitting between FC and ZFC is observed. The shoulder features at T_s in Figs. 4–7 are no longer present. The $M(B)$ loop shows no displacement around the origin (h).

frustration due to the presence of mixed ferromagnetic (FM) and antiferromagnetic (AF) exchange (cf. Sec. V).

The second feature is the appearance of a peak in the form of a shoulder at temperatures around 70–90 K denoted as T_s in Figs. 4–7. The shoulder feature is less pronounced for sample S1 and becomes more distinct in samples S2–S5. For S1 and S2, the feature becomes smeared out as of the 3 T measuring field and is not observable at 5 T. For samples S1–S5, the feature is distinct in 1 T and is observable up to 5 T measuring field in samples S3 and S4. The position of T_s, determined visually as the temperature corresponding to the peak does not change when measuring on cooling and warming, and there is no ZFC-FC splitting at T_s. The absence of a splitting at T_s suggests the absence of any magnetic frustration and that this feature is related to the onset of AF ordering as will be further discussed in Sec. V.

$M(B)$ at 10 K of all samples shown in Figs. 4(f)–9(f) exhibit a high-field susceptibility arising from coexisting AF and FM exchange. For samples S1 and S2, the $M(B)$ curves

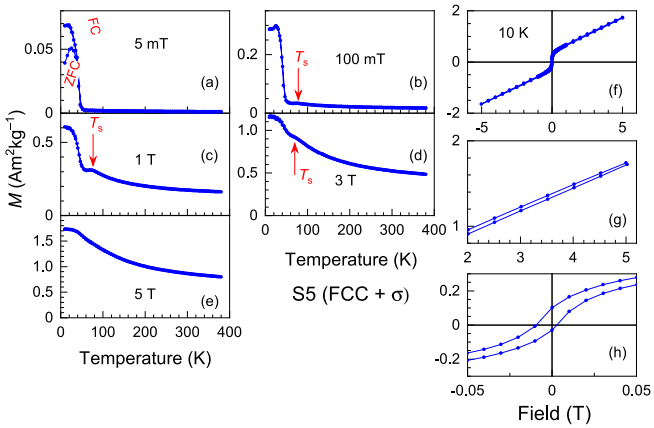

FIG. 8. $M(T)$ under 5 mT external field obtained under ZFC and FC conditions for S5. (a) 5 mT, (b) 100 mT, (c) 1 T, (d) 3 T, and (e) 5 T. The shoulder features at T_s in Figs. 4–7 are no longer present. The $M(B)$ loop shows no displacement around the origin (h).

at 10 K in Figs. 4(f) and 5(f), respectively, do not show a retracing hysteresis at the positive- and negative-field high-field ends so that these curves are essentially minor loops. The nonretracing feature is shown in detail in Figs. 4(g) and 5(g). Being so, the low-field expanded region of the curves in Figs. 4(h) and 5(h) are shifted vertically and horizontally. Similar curves in Figs. 6(f) and 7(f) do retrace better at high fields as seen in Figs. 6(g) and 7(g), but the loops in Figs. 6(h) and 7(h) are still shifted both vertically and horizontally which would suggest the presence of magnetic pinning effects in these cases. This would then imply that the behavior of the curves in Figs. 4(h) and 5(h) could also be partially due to exchange bias and other magnetic pinning effects as well.

For $M(T)$ of the sample S6 shown in Figs. 9(a)–9(d), low-temperature freezing is practically no longer observed, and along with it, the shoulder feature also vanishes implying that AF exchange is not present in S6. For this sample, the $M(B)$ data points retrace at high-field ends as seen in Fig. 9(g), and no shift in the magnetization loop is observed [Fig. 9(h)]. The absence of shifts is due to the absence of the source of pinning, namely the AF exchange. T_s is also absent for this sample.

To be able to account for the various magnetic couplings at low temperatures, we plot in Fig. 10 T_s as a function of the measuring field and, in Fig. 11, $M(B)$ at various temperatures for sample S2 around T_f and T_s.

We see in Fig. 10 that T_s for S2–S5 depends on the chemical composition as well as the measuring field. T_s essentially decreases with increasing field for all compositions. T_s of S1 cannot be determined with the same accuracy as for the others, as for this sample a cusp in $M(T)$ is less clear than for samples S2–S5. Although there appears to be a systematic decrease of T_s with increasing field, we do not see a systematic arrangement of the curves at any particular field. This could be due to variations in the concentration of any one of the species enhancing or weakening the AF exchange, thus leading to a higher or lower T_s, respectively.

Figure 11 shows the results of $M(B)$ measurements for S2 at temperatures corresponding to $T < T_f$ [10 and 30 K, Figs. 11(a) and 11(b)], $T_f < T < T_s$ [45 and 60 K, Figs. 11(c)

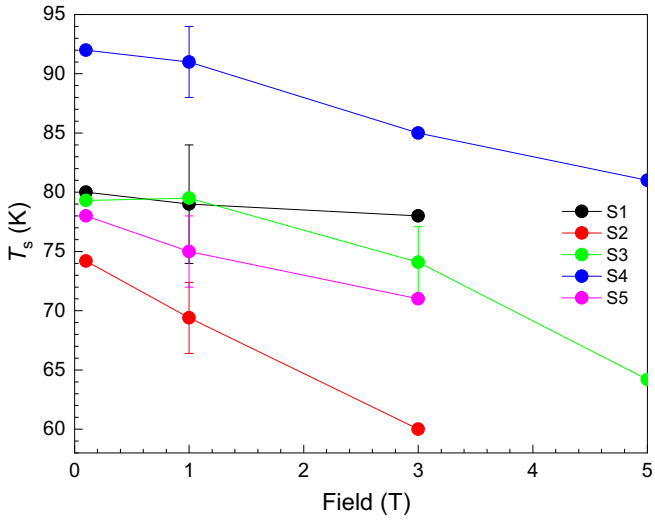

FIG. 10. The field dependence of Ts for S1, S2, S3, and S4.

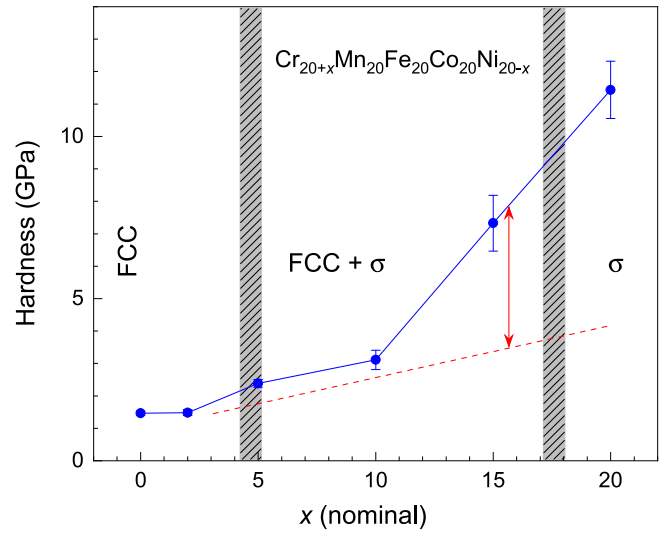

FIG. 12. The nominal composition dependence of the hardness measured at room temperature. The red dashed line is an extrapolation from the fcc range to $x \geqslant 10$. The difference between the red dashed line and the blue data, representing the data for S4, S5, and S6, is the contribution from the σ phase.

and 11(d)], and $T > T_s$ [75 and 150 K, Fig. 11(e)]. In Fig. 11(f), $M(T)$ in the range $10 \leqslant T \leqslant 100$ is also shown, and the temperatures at which the measurements have been carried out are marked with arrows. At 10 and 30 K, low-field features related to FM ordering can be seen. Since at 45 K this feature is absent, the FM ordering can be occurring below a T_C of about 40 K. Together with the AF coupling occurring below T_s, the state at low temperatures below $T_f \approx 30$ K becomes a glassy frustrated state. All alloys have similar T_Cs and T_fs as can be extracted from the 5 mT measurements in Figs. 4(a)–9(a).

D. Hardness

The hardness of the samples was measured ten times from different regions, and the average value and the standard deviations were obtained. Figure 12 shows the hardness as a function of the nominal Cr content. Cr is harder than the other constituent elements, so that it should cause the hardness of the sample to steadily increase as its content increases within a given crystallographic phase. Since S1 and S2 corresponding to $x = 0$ and $x = 2$, respectively, are both fcc, there is little variation in the hardness. Some increase in the hardness begins to occur at $x = 5$, but as of $x = 10$, the increase becomes faster as the amount of σ phase increases. The red dashed line guides the composition dependence of the hardness extrapolated from the fcc range. The difference between the dashed line and the blue line representing the data for S4, S5, and S6 is the contribution from the harder σ phase.

The presence of a moment-volume instability leads to an enhanced anharmonicity that causes the second derivative of the binding energy with respect to the atomic volume, namely the bulk modulus, to become smaller than for a similar material without a moment-volume instability. The presently investigated alloy series shows a gradual structural transition from the fcc to the σ phase and thereby a transition from a system with a moment-volume instability in the ground state to a system without one. This causes the rapid increase of the hardness at room temperature around a nominal composition where the amount of σ phase becomes substantial.

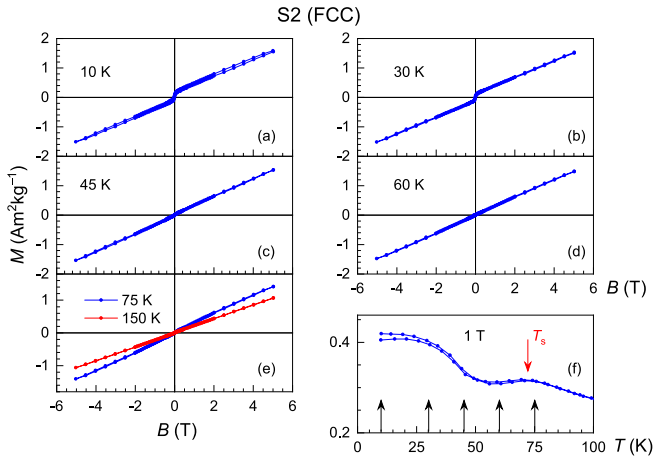

FIG. 11. $M(B)$ at temperatures $T < T_f$, $T_f < T < T_s$, and $T > Ts$. The vertical black arrows mark the temperature positions of the $M(B)$ measurements. T_s is also given.

V. DISCUSSION

A. Low-temperature magnetic ordering

There are common structural and magnetic properties of the high-entropy Cantor-alloy and fcc-Fe as summarized in Sec. I. The common property is that for both of these materials $(e/a) = 8$ and both exhibit the anti-Invar property [12] suggesting that their ground-state properties could be similar. This would mean that the Cantor alloy could exhibit antiferromagnetism at low temperatures as predicted and observed for fcc-Fe [14,43]. We take advantage of the fact that in the case of the Cantor alloy, the constituent elements lie close to one another in the periodic regime of the elements allowing (e/a)

to be a governing parameter of the physical properties of both the Cantor alloy and fcc-Fe.

For the Cantor alloy there are two distinct features in $M(T)$ at low temperatures as pointed out in Ref. [13]: one around 40 K and the other around 90 K. The authors of this reference had interpreted the feature around 90 K, which we have labeled as T_s, to be related to a transition to a super spin-glass state. However, we do not find a splitting between ZFC and FC $M(T)$ curves at this temperature that would be an indication for a glassy state. Instead, the ZFC and FC curves retrace perfectly around 90 K and feature a cusp that can be identified as a Néel temperature related to AF ordering.

Further support for the presence of AF ordering at T_s comes from the vertically shifted $M(B)$ loops in samples S1–S4 and for the sample studied in Ref. [13]. The vertical shift occurs at $T < T_C$. Its direction is governed by the direction of the cooling field, and it results from the presence of moments pinned in the direction of the cooling field. The pinning requires an AF exchange that either surrounds or is in the proximity of the FM components. The presence of AF exchange can then be accounted for if T_s is actually a Néel temperature. For the pure σ-phase sample S6, neither a T_s nor substantial bifurcation in the ZFC and FC curves below T_f, nor vertically shifted $M(B)$ loops, can be identified, so that AF exchange is weak in this sample. The only remaining factor in favor for the presence of AF exchange is the high-field susceptibility at 10 K observed in $M(B)$.These observations support the fact that T_s is related to the onset of AF ordering at these (e/a)s and is a property of the fcc phase.

One further evidence for AF ordering below T_s is the essentially linear $M(B)$ measured at 45 and 60 K for sample S2 shown in Figs. 11(c) and 11(d), respectively. The linear behavior is not in accordance with a super spin-glass state, which would have exhibited a nonlinear $M(B)$.

AF ordering has been observed in fcc-Fe precipitates in Cu as well as in fcc-steels [14,43]. Diffuse magnetic neutron scattering experiments on such a material $Fe_{77}Ni_{13}Mn_7C_3$ with $(e/a) = 8.25$ have revealed the presence of AF ordering below 100 K [44]. At high temperatures, in the paramagnetic regime, they have also provided evidence for the strengthening of FM correlations with increasing temperature up to 1150 K demonstrating the anti-Invar property of such materials. Presently, diffuse magnetic neutron scattering experiments on the Cantor alloy have not been reported, so that direct evidence for low-temperature AF ordering and strengthening FM correlations with increasing temperature has not been given. Such experiments are planned. Presently, the evidence we can provide here is through the thermal expansion and magnetization properties.

The nature of the ordering below 45 K is less a structural issue since we see that it occurs both in the fcc and in the σ phases at nearly the same temperature, and we see that structure does not change at this temperature. $M(B)$ obtained at 10 K for all samples show a FM response in small fields followed by a continued linear increase with no tendency to saturate. The splitting between the FC and ZFC curves persists up to 5 T for the equiatomic alloy S1 indicating that the AF exchange at $T < 45$ K remains strong. This is also the case for sample S2, though the splitting at the higher fields become somewhat weaker. The splitting at measuring fields higher than 5 mT are absent in all other samples S3–S6 due to the weakening of AF exchange as the σ phase emerges, thus facilitating the spins to align with low external fields under both FC and ZFC conditions. However, AF exchange is not totally absent in these samples at low temperatures as also evidenced from the continued linear increase of $M(B)$ at high fields. At this point we can only suggest that the rapid increase in the magnetization below 40 K is due to the introduction of additional FM exchange. In addition to these interactions, for S1–S4, long-range AF ordering should also be present at $T < Ts$, prevailing to below T_f, in addition to local FM ordering. Further polarized neutron diffraction studies are required to clarify these points

B. The thermal expansion

The temperature dependence of the thermal expansion of $3d$ metals and alloys can provide clues to the nature of their ground-state properties. A regular thermal expansion complies to the Grüneisen model. Cubic solids expand about 7%–8% in volume before melting. fcc-Fe does not comply to this model and expands to about 12% within its stability range $1184 \leqslant T \leqslant 1665$ K. The cause for this is related to the enhanced anharmonicity provided by the presence of moment-volume instabilities in its ground state: A FM high-moment–high-volume state lies energetically higher by about 10 meV than the AF low-volume–low-moment equilibrium state [35]. This provides the enhanced anharmonicity towards larger volumes giving rise to the enhanced thermal expansion, otherwise referred to as the anti-Invar effect [42]. This argument can also be reversed so that the presence of a moment-volume instability in the ground state causing an enhanced anharmonicity can be anticipated if a measured thermal expansion of a material is larger-than-normal.

In the case of the Cantor alloy with $(e/a) = 8$, we had shown that an enhanced anharmonicity provided by the presence of a FM state at volumes beyond the equilibrium AF state can be expected so that the feature around T_s in $M(T)$ data in this study can be expected to be related to AF ordering. On the other hand, the sample S6 is in the pure σ state and shows a regular behavior in the thermal expansion so that a moment-volume instability, and therefore, the presence of multiple magnetic states in the ground state leading to large thermal spin fluctuations is not expected. Indeed, a feature like the one at T_s for the fcc-incorporating alloys is absent in the σ-phase sample. The case is similar for S5, for which the σ phase is dominant and any effect from the fcc phase is masked. These arguments provide support for identifying the feature at T_s to be related to antiferromagnetic ordering.

C. The σ phase

One of the interesting structural properties of $3d$ HEAs is the formation of the σ phase in the range $6.9 < (e/a) < 7.3$ [28,29,45]. This falls into the range where Fe-Cr, Fe-V, and Mn-V alloys also exhibit the σ phase. It is also the range within which Mn and binary $3d$-Mn alloys form complex cubic A12 (α-Mn) and A13 (β-Mn) phases with 58 and 20 atoms per unit cell, respectively. These are summarized in Fig. 13.

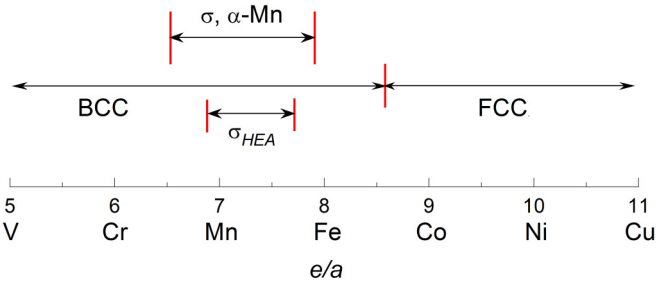

FIG. 13. Structural stability ranges shown as a sketch over an e/a axis. The ranges bounded by the red lines are for the complex phases α-Mn and σ. The σ stability range for HEAs is indicated as σ_{HEA}.

σ, A12, and A13 complex phases appear to be occurring in an e/a range corresponding to the crossover from the stability range of the bcc phase to the fcc phase raising the question as to whether these phases result from electronic frustration due to interactions related to competing fcc and bcc phase stabilities. The fact that the σ phase also occurs at boundaries between fcc and bcc grains in some steels is also supportive for this argument [46].

VI. CONCLUSIONS

We have studied the structural and magnetic properties of off-equiatomic $Cr_{20+x}Mn_{20}Fe_{20}Co_{20}Ni_{20-x}$ with nominal compositions $x = 0, 2, 5, 10, 15$, and 20 to understand the nature of the low-temperature magnetic interactions in the fcc and σ phase and their stability ranges of the structures. The σ phase tends to stabilize for $x > 2$ as a mixture with the fcc phase and appears as a single phase for $x = 20$. The sample $x = 0$ is the fcc equiatomic alloy with $e/a = 8$ and shows practically identical properties as fcc-Fe. We provide an argument here that the low-temperature anomaly seen at 90 K for $x = 0$ is related to antiferromagnetic ordering expected for a $3d$ fcc alloy with $(e/a) = 8$. The same anomaly is observed up to $x = 10$, whereby the transition temperature decreases with increasing x. The argument is based on the expected presence of moment-volume instabilities at these compositions as in fcc-Fe.

We observe spin freezing below T_f for all samples, for which the freezing is strong for $x = 0$ and $x = 2$ seen by the persistence of the ZFC-FC splitting up to the highest fields. The anisotropy of the expected long-range AF ordering in these two samples can be large enough so that the splitting is not lifted even at high fields. Freezing is also found in all other samples, however only at low fields and is practically absent for the $x = 20$, the pure σ-phase sample. In these cases, the anisotropy of the AF ordering persisting to below T_f is weak, or the ordering is not observed at all as for $x > 10$.

The σ-phase stability range lies within the compositional limits of the range known for $3d$-alloys. The complex unit cell of the σ phase as well as the A12 and A13 structures of Mn suggest that these phases could result out of structural frustration.

ACKNOWLEDGMENTS

We acknowledge the support of Deutsche Forschungsgemeinschaft (Project No. 405553726-CRC/TRR 270) and the TUBITAK Science Fellowships and Grant Programs (Grant No. 1059B192000916).

[1] B. Cantor, I. T. H. Chang, P. Knight, and A. J. B. Vincent, Microstructural development in equiatomic multicomponent alloys, Mater. Sci. Eng. A **375-377**, 213 (2004).
[2] J.-W. Yeh, S.-K. Chen, S.-J. Lin, J.-Y. Gan, T.-S. Chin, T.-T. Shun, C.-H. Tsau, and S.-Y. Chang, Nanostructured high-entropy alloys with multiple principal elements: Novel alloy design concepts and outcomes, Adv. Eng. Mater. **6**, 299 (2004).
[3] Y. Zou, H. Ma, and R. Spolenak, Ultrastrong ductile and stable high-entropy alloys at small scales, Nat. Commun. **6**, 7748 (2015).
[4] B. Gludovatz, A. Hohenwarter, D. Catoor, E. H. Chang, E. P. George, and R. O. Ritchie, A fracture-resistant high-entropy alloy for cryogenic applications, Science **345**, 1153 (2014).
[5] H. Kou, J. Lu, and Y. Li, High-strength and high-ductility nanostructured and amorphous metallic materials, Adv. Mater. **26**, 5518 (2014).
[6] C. P. Lee, Y. Y. Chen, C. Y. Hsu, J. W. Yeh, and H. C. Shih, The effect of boron on the corrosion resistance of the high entropy alloys $Al_{0.5}CoCrCuFeNiB_x$, J. Electrochem. Soc. **154**, C424 (2007).
[7] M. C. Troparevsky, J. R. Morris, P. R. C. Kent, A. R. Lupini, and G. M. Stocks, Criteria for Predicting the Formation of Single-Phase High-Entropy Alloys, Phys. Rev X. **5**, 011041 (2015).
[8] G. Qin, R. Chen, H. Zheng, H. Fang, L. Wang, Y. Su J. Guo, and H. Fu, Strengthening fcc-CoCrFeMnNi high entropy alloys by Mo addition, J. Mater. Sci. Technol. **35**, 578 (2019).
[9] Y. F. Ye, Q. Wang, J. Lu, C. T. Liu, and Y. Yang, High-entropy alloy: challenges and prospects, Mater. Today **19**, 349 (2016).
[10] D. B. Miracle and O. N. Senkov, A critical review of high entropy alloys and related concepts, Acta Mater. **122**, 448 (2017).
[11] E. P. George, D. Raabe, and R. O. Ritchie, High-entropy alloys, Nat. Rev. Mater. **4**, 515 (2019).
[12] M. Acet, Inducing strong magnetism in $Cr_{20}Mn_{20}Fe_{20}Co_{20}Ni_{20}$ high-entropy alloys by exploiting its anti-Invar property, AIP Adv. **9**, 095037 (2019).
[13] O. Schneeweiss, M. Friák, M. Dudová, D. Holec, M. Sob, D. Kriegner, V. Holý, P. Beran, E. P. George, J. Neugebauer, and A. Dlouhý, Magnetic properties of the CrMnFeCoNi high-entropy alloy, Phys. Rev. B **96**, 014437 (2017).
[14] U. Gonser, C. J. Meechan, A. H. Muir, and H. Wiedersich, Determination of Néel temperatures in fcc iron, J. Appl. Phys. **34**, 2373 (1963).
[15] D. Ma, B. Grabowski, F. Körmann, J. Neugebauer, and D. Raabe, Ab initio thermodynamics of the CoCrFeMnNi high entropy alloy: Importance of entropy contributions beyond the configurational one, Acta Mater. **100**, 90 (2015).
[16] Z. Dong, S. Schönecker, W. Li, D. Chen, and L. Vitos, Thermal spin fluctuations in CoCrFeMnNi high entropy alloy, Sci. Rep. **8**, 12211 (2018).

[17] C. L. Tracy, S. Park, D. R. Rittman, S. J. Zinkle, H. Bei, M. Lang, R. C. Ewing, and W. L. Mao, High pressure synthesis of a hexagonal close-packed phase of the high-entropy alloy CrMnFeCoNi, Nat. Commun. **8**, 15634 (2017).

[18] G. Laplanche, P. Gadaud, O. Horst, F. Otto, G. Eggeler, and E. P. George, Temperature dependencies of the elastic moduli and thermal expansion coefficient of an equiatomic, single-phase CoCrFeMnNi high-entropy alloy, J. Alloys Compd. **623**, 348 (2015).

[19] D. Billington, A. D. N. James, E. I. Harris-Lee, D. A. Lagos, D. O'Neill, N. Tsuda, K. Toyoki, Y. Kotani, T. Nakamura, H. Bei, S. Mu, G. D. Samolyuk, G. M. Stocks, J. A. Duffy, J. W. Taylor, S. R. Giblin, and S. B. Dugdale, Bulk and element-specific magnetism of medium-entropy and high-entropy Cantor-Wu alloys, Phys. Rev. B **102**, 174405 (2020).

[20] P. Koželj, S. Vrtnik, M. Krnel, A. Jelen, D. Gacnik, M. Wencka, Z. Jaglicice, A. Meden, F. Danoix, J. Ledieu, M. Feuerbacher, and J. Dolinsek, Spin-glass magnetism of the non-equiatomic CoCrFeMnNi high-entropy alloy, J. Magn. Magn. Mater. **523**, 167579 (2021).

[21] J. Šebesta, K. Carva, and D. Legut, Evolution of the Curie temperature for a substituted Cantor alloy, Phys. Rev. B **103**, 064407 (2021).

[22] S. Huang, E. Holmström, O. Eriksson, and L. Vitos, Mapping the magnetic transition temperatures for medium- and high-entropy alloys, Intermetallics **95**, 80 (2018).

[23] V. Chaudhary, R. Chaudhary, R. Banerjee, and R. V. Ramanujan, Accelerated and conventional development of magnetic high entropy alloys, Mater. Today **49**, 231 (2021).

[24] N. Tang, L. Quigley, W. L. Boldman, C. S. Jorgensen, R. Koch, D. O'Leary, H. R. Medal, P. D. Rack, and D. A. Gilbert, Magnetism in metastable and annealed compositionally complex alloys, Phys. Rev. Mater. **5**, 114405 (2021).

[25] F. Tian, L. Karoly Varga, N. Chen, L. Delczeg, and L. Vitos, *Ab initio* investigation of high-entropy alloys of 3*d* elements, Phys. Rev. B **87**, 075144 (2013).

[26] Z. Rao, B. Dutta, F. Körmann, D. Ponge, L. Li, J. He, L. Stephenson, L. Schäfer, K. Skokov, O. Gutfleisch, D. Raabe, and Z. Li, Unveiling the mechanism of abnormal magnetic behavior of FeNiCoMnCu high-entropy alloys through a joint experimental-theoretical study, Phys. Rev. Mater. **4**, 014402 (2020).

[27] C. C. Hsieh and W. Wu, Overview of intermetallic sigma (σ) phase precipitation in stainless steels, ISRN Metallurgy **2012**, 732471 (2012).

[28] M.-H. Tsai, H. Yuan, G. Cheng, W. Xu, W. W. Jian, M.-H. Chuang, C.-C. Juan, A.-C. Yeh, S.-J. Lin, and Y. Zhu, Significant hardening due to the formation of a sigma phase matrix in a high entropy alloy, Intermetallics **33**, 81 (2013).

[29] M.-H. Tsai, K.-Y. Tsai, C.-W. Tsai, C. Lee, C.-C. Juan, and J-W. Yeh, Criterion for sigma phase formation in Cr- and V-containing high-entropy alloys, Mater. Res. Lett. **1**, 207 (2013).

[30] M.-H. Tsai, K.-C. Chang, J.-H. Li, R.-C. Tsai, and A.-H. Cheng, A second criterion for sigma phase formation in high-entropy alloys, Mat. Res. Lett. **4**, 90 (2015).

[31] G. L. S. Berglund, C. Reinhart, A. Kostka, F. Fox, and E. P. George, Phase stability and kinetics of σ-phase precipitation in CrMnFeCoNi high-entropy alloys, Acta Mater. **161**, 338 (2018).

[32] F. Otto, A. Dlouhý, K. G. Pradeep, M. Kuběnov, D. Raabe, G. Eggeler, and E. P. George, Decomposition of the single-phase high-entropy alloy CrMnFeCoNi after prolonged anneals at intermediate temperatures, Acta Mater. **112**, 40 (2016).

[33] E. J. Pickering, R. Muñoz-Moreno, H. J. Stone, and N. G. Jones, Precipitation in the equiatomic high-entropy alloy CrMnFeCoNi, Scr. Mater. **113**, 106 (2016).

[34] Y. Sumitomo, T. Moriya, H. Ino, and F. E. Fujita, The Mossbauer effect of Fe-V and Fe-Cr sigma phase, J. Phys. Soc. Jpn. **35**, 461 (1973).

[35] V. L. Moruzzi, Magnetovolume instabilities and ferromagnetism versus antiferromagnetism in bulk fcc iron and manganese, Phys. Rev. B **39**, 6957 (1989).

[36] Z. Rao, A. Çakır, Ö. Özgün, D. Ponge, D. Raabe, Z. Li, and M. Acet, *3d* transition-metal high-entropy Invar alloy developed by adjusting the valence-electron concentration, Phys. Rev. Mater. **5**, 044406 (2021).

[37] M. Acet, B. Gehrmann, E. F. Wassermann, H. Bach, and W. Pepperhoff, Relevance of magnetic instabilities to the properties of interstitial solid solutions and compounds of Fe, J. Magn. Magn. Mater. **232**, 221 (2001).

[38] A. Çakır, L. Righi, F. Albertini, M. Acet, and M. Farle, Intermartensitic transitions and phase stability in $Ni_{50}Mn_{50-x}Sn_x$ Heusler alloys, Acta Mater. **99**, 140 (2015).

[39] V. Petříček, M. Dusek, and L. Palatinus, Crystallographic computing system JANA2006: General features, Z. Kristallogr. **229**, 345 (2014).

[40] T. Faske and W. Donner, X-ray diffractometer for the investigation of temperature- and magnetic field-induced structural phase transitions, J. Appl. Crystallogr. **51**, 761 (2018).

[41] J. Rodríguez-Carvajal, Recent advances in magnetic structure determination by neutron powder diffraction, Phys. B: Condens. Matter **192**, 55 (1993).

[42] M. Acet, H. Zähres, E. F. Wassermann, and W. Pepperhoff, High-temperature moment-volume instability and anti-Invar of γ-Fe, Phys. Rev. B **49**, 6012 (1994).

[43] Y. Tsunoda, N. Kunitomit, and R. M. Nicklow, Magnetic structure of γ-Fe precipitates in a Cu matrix, J. Phys. F: Met. Phys. **17**, 2447 (1987).

[44] M. Acet, E. F. Wassermann, K. H. Andersen, J. Kulda, A. P. Murani, and A. Wildes, Large spin fluctuations and moment-volume coupling in Fe in an FCC environment, Phys. B: Condens. Matter **276-278**, 728 (2000).

[45] S. Guo, C. Ng, J. Lu, and C. T. Liu, Effect of valence electron concentration on stability of fcc or bcc phase in high entropy alloys, J. Appl. Phys. **109**, 103505 (2011).

[46] D. M. E. Villanueva, F. C. P. Junior, R. L. Plaut, and A. F. Padilha, Comparative study on sigma phase precipitation of three types of stainless steels: Austenitic, superferritic and duplex, Mater. Sci. Technol. **22**, 1098 (2006).